



This is a repository copy of *Impact of rare earth ion size on the phase evolution of MoO₃-containing aluminoborosilicate glass-ceramics*.

White Rose Research Online URL for this paper:
<http://eprints.whiterose.ac.uk/135748/>

Version: Accepted Version

Article:

Patil, D.S., Konale, M., Gabel, M. et al. (6 more authors) (2018) Impact of rare earth ion size on the phase evolution of MoO₃-containing aluminoborosilicate glass-ceramics. *Journal of Nuclear Materials*, 510. pp. 539-550. ISSN 0022-3115

<https://doi.org/10.1016/j.jnucmat.2018.08.004>

Reuse

This article is distributed under the terms of the Creative Commons Attribution-NonCommercial-NoDerivs (CC BY-NC-ND) licence. This licence only allows you to download this work and share it with others as long as you credit the authors, but you can't change the article in any way or use it commercially. More information and the full terms of the licence here: <https://creativecommons.org/licenses/>

Takedown

If you consider content in White Rose Research Online to be in breach of UK law, please notify us by emailing eprints@whiterose.ac.uk including the URL of the record and the reason for the withdrawal request.



eprints@whiterose.ac.uk
<https://eprints.whiterose.ac.uk/>

1 **Impact of Rare Earth Ion Size on the Phase Evolution of MoO₃-Containing**
2 **Aluminoborosilicate Glass-Ceramics**

3 Deepak S. Patil^{1,2}, Manisha Konale^{1,3}, Mathew Gabel⁴, Owen K. Neill⁵, Jarrod Crum⁶, Ashutosh
4 Goel⁷, Martin Stennett,⁸ Neil C. Hyatt,⁸ John S. McCloy^{1,2,6#}

5 ¹School of Mechanical & Materials Engineering, Washington State University, Pullman, WA 99164,
6 USA

7 ²Materials Science & Engineering Program, Washington State University, Pullman, WA 99164, USA

8 ³Department of General and Inorganic Chemistry and CEMNAT, Faculty of Chemical Technology,
9 University of Pardubice, Studentska 95, Pardubice, 53210, Czech Republic

10 ⁴Department of Physics and Astronomy, Washington State University, Pullman, Washington 99164-2814,
11 USA

12 ⁵Electron Microbeam Analysis Lab, School of Earth and Environmental Sciences, University of
13 Michigan, Ann Arbor, Michigan, 48109-1005, USA

14 ⁶Pacific Northwest National Laboratory, P.O. Box 999, Richland, Washington 99352, USA

15 ⁷Department of Materials Science and Engineering, Rutgers – The State University of New Jersey,
16 Piscataway, New Jersey, USA

17 ⁸Department of Materials Science and Engineering, the University of Sheffield, S1 3JD, UK

18
19 Corresponding author:

20 [#john.mccloy@wsu.edu](mailto:john.mccloy@wsu.edu); Phone +1 509-335-7796; Fax +1 509-335-4662

21

22

23 Abstract

24 Transition metal and rare earth cations are important fission products present in used nuclear
25 fuel, which in high concentrations tend to precipitate crystalline phases in vitreous nuclear waste
26 forms. Two phases of particular interest are powellite (CaMoO_4) and oxyapatite
27 ($\text{Ca}_2\text{RE}_8(\text{SiO}_4)_6\text{O}_2$). The glass compositional dependencies controlling crystallization of these
28 phases on cooling from the melt are poorly understood. In the present study, the effect of rare
29 earth identity and modifier cation field strength on powellite and apatite crystallization were
30 studied in a model MoO_3 -containing alkali/alkaline-earth aluminoborosilicate glass with focus on
31 (1) influence of rare earth cation size (for RE^{3+} : Ce, La, Nd, Sm, Er, Yb) and (2) influence of
32 non-framework cations (RE^{3+} , Mo^{6+} , Na^+ , Ca^{2+}). Quenched glasses and glass-ceramics (obtained
33 by slow cooling) were characterized by X-ray diffraction (XRD), Raman spectroscopy, X-ray
34 absorption (XAS), and electron probe microanalysis (EPMA). All samples were X-ray
35 amorphous upon quenching, except the Ce-containing composition which crystallized ceria
36 (CeO_2), and the sample devoid of any rare earth cations which crystallized powellite (CaMoO_4).
37 On heat treatment, powellite and oxyapatite crystallized in the majority of the samples with the
38 former crystallizing in the volume, while the latter on the surface. The EPMA results confirmed
39 a small concentration of boron in the oxyapatite crystal structure. RE cations were incorporated
40 in the glass, as well as in powellite, oxyapatite, and in the case of Yb^{3+} , keiviite ($\text{Yb}_2\text{Si}_2\text{O}_7$).
41 Raman spectroscopy showed that the primary vibration band for molybdate MoO_4^{2-} in the
42 glasses was strongly affected by the ionic field strength of the modifying cations (alkali, alkaline
43 earth, and RE), suggesting their proximity to the MoO_4^{2-} ions in the glass, though the Mo-O bond
44 length and coordination according to XAS suggested little local change.

45 **Keywords:** Rare earth ions, nuclear waste immobilization, molybdate, glass-ceramic

46 **1 Introduction**

47 Borosilicate glasses are one of the most suitable matrices for immobilization of nuclear
48 waste worldwide due to their high nuclear waste loading capacity, low tendency for
49 crystallization, high chemical durability, and high self-irradiation resistance [1]. Nuclear waste
50 from reprocessing of used nuclear fuel (UNF) contains a large variety of fission products,
51 including large quantities of the rare-earth (RE) and transition metals (TM), with molybdenum
52 being a particularly problematic due to its high fission yield and low solubility in borosilicate
53 glass [2]. In some countries, the research effort is directed towards the development of glass
54 waste form with no crystallization, or at least minimal crystallization of only durable phases [3].
55 Another suggested approach being pursued is the development of a glass-ceramic waste form of
56 a desired phase assemblage by controlled crystallization, thus leading to higher waste loading
57 and superior chemical durability in comparison to its glassy counterpart [4-8]. Two crystalline
58 phases of particular interest are powellite (CaMoO_4) and oxyapatite (nominally
59 $\text{Ca}_2\text{RE}_8(\text{SiO}_4)_6\text{O}_2$), which are the primary crystalline phases accommodating Mo and RE ions in
60 these nuclear waste glass-ceramic systems [5].

61 **1.1 Molybdenum in borosilicate glass and glass-ceramics**

62 In order to design a borosilicate-based glassy waste form, it is imperative to understand the
63 compositional and structural drivers governing the solubility of molybdenum oxides in the
64 relevant glass chemistries. Based on the existing literature [9-11], the solubility of MoO_3 in alkali
65 borosilicate glasses is limited to ~1 mass% when no rare earth ions are present (see below) [12].
66 This threshold limit of MoO_3 solubility affects the total loading of HLW into the base glass
67 matrix, which leads to the increase of the total volume of the vitrified waste. Depending on the
68 specific waste stream the maximum waste loading may be as low as ~18 mass%. Higher amounts
69 of MoO_3 (>1 mass%) in borosilicate glass is known to induce phase separation and

70 crystallization [10, 13]. The phase separation and crystallization of Mo phases can have a
71 deleterious effect on the durability and safety of the vitrified waste. For compositions rich in
72 alkali, MoO₃ usually phase separates and crystallizes as an alkali molybdate (i.e., Na₂MoO₄)
73 which is soluble in water [14]. Also, the alkali ions in Na₂MoO₄ can be partially or fully replaced
74 by other alkali cations (short-lived ¹³⁷Cs or long-lived ¹³⁵Cs) resulting in water-soluble alkali
75 molybdates such as Cs₃Na(MoO₄)₂, CsNaMoO₄·2H₂O and Cs₂MoO₄ [14-16]. It is known that
76 the distribution of Na⁺ in the glass can be controlled, such as with Al₂O₃, B₂O₃ and CaO, thus
77 forcing molybdate to partition and crystallize powellite (CaMoO₄) which is more durable in
78 water than alkali molybdates [10, 17].

79 In alkali borosilicate glasses, the molybdenum cation exists primarily in +6 oxidation state
80 (as molybdate oxyanion), and in the dilute limit as an MoO₄²⁻ tetrahedron, based on evidence
81 from Mo K-edge X-ray absorption [18, 19], and molybdate vibrational frequency changes with
82 the average charge density of modifier [19]. Molybdate oxyanions are thought to be located in
83 the depolymerized region of the glass structure surrounded by alkali and alkaline-earth cations
84 [12]. Recent ab initio molecular dynamics simulations have shown that when Li⁺ is substituted
85 for Na⁺, however, some longer Mo-O bonds result in connection with the borosilicate network
86 and an effective Mo⁵⁺ charge [20].

87 1.2 Rare earth cations (RE³⁺) in borosilicate glass and glass-ceramics

88 Molybdate and RE ions interact strongly in borosilicate glasses, with the latter exerting a
89 significant impact on the solubility of former (increases to 3 – 5 mass%) in the glass structure
90 [1, 21]. However, the mechanism of their interaction resulting in higher solubility of
91 molybdenum in borosilicate glasses is still debated [11]. The most well-known hypothesis is the
92 close relationship between RE³⁺ and [MoO₄]²⁻ tetrahedral entities in the depolymerized region of
93 the glassy network, where the RE³⁺ ions tend to disperse any molybdate clusters leading to an

94 increase in the molybdenum solubility in the glassy waste form. On the contrary, the removal of
95 RE^{3+} from the glassy matrix (for example, by crystallization of rare-earth containing oxyapatite
96 phase) results in the crystallization of alkali/alkaline-earth molybdate phases [1, 21, 22]. Further,
97 both RE (Nd, Gd, etc.) [10, 23-25] and actinide ions [26] can be incorporated in the powellite
98 crystal structure, as well as the related Na-Nd molybdate scheelite structure [27, 28].

99 The sequence of crystallization of oxyapatite and powellite is highly dependent on
100 several parameters. Generally, for a glass containing both MoO_4^{2-} and RE^{3+} , the crystallization
101 (upon heating from room temperature) initiates through the formation of powellite in the volume
102 followed by oxyapatite on the surface [21], while this sequence reverses during crystallization
103 from the melt under slow cooling [11]. In fact, molybdate crystalline phases (Na_2MoO_4 ,
104 CaMoO_4) have been suggested as nucleation sites for apatite crystals [21]. However, as
105 mentioned above, this sequence of crystalline phase assemblage is subject to change based on the
106 glass/melt chemistry and thermal conditions.

107 Most studies of oxyapatite crystallization in nuclear waste glass have focused on Nd_2O_3
108 as the primary RE oxide addition, and the phase produced is $\text{Ca}_2\text{Nd}_8(\text{SiO}_4)_6\text{O}_2$ [1, 2, 4, 29]. The
109 stoichiometry of this phase is variable, with a tendency to be Ca-rich, Nd-poor, and O-poor, i.e.,
110 $\text{Ca}_{2+x}\text{Nd}_{8-x}(\text{SiO}_4)_6\text{O}_{2-0.5x}$ [30, 31], though likely the stoichiometric range is quite large, including
111 Ca-absent Nd-only versions of the crystal [32]. The $\text{Ca}_2\text{Nd}_8(\text{SiO}_4)_6\text{O}_2$ oxyapatite has been well-
112 studied for radiation damage due to its chemical and structural similarity to target phases for
113 actinide immobilization [33, 34].

114 The composition of RE oxyapatite can be quite variable, and many synthetic pure phase
115 RE oxyapatites have been reported containing Ca (or Ba, Sr, Mg, or Pb), including La, Nd, Sm,
116 Dy, Er, Lu, as well as Y [35]. Several studies have been conducted looking at the compositions

117 of oxyapatites crystallizing from the simulated nuclear waste glass. In complicated starting glass
118 compositions, energy dispersive spectroscopy (EDS) has shown that multiple RE cations, for
119 example, Y^{3+} , La^{3+} , Ce^{3+}/Ce^{4+} , Pr^{3+} , Nd^{3+} , Sm^{3+} , along with alkali (for example, Na^+), and
120 alkaline earth ions (for example, Ca^{2+} , Sr^{2+}) can simultaneously incorporate into the oxyapatite
121 structure [5]. In comparing La, Nd, and La+Nd in Na-Ca aluminoborosilicate glasses, it was
122 observed that the amount of RE_2O_3 that could be accommodated in the glass before apatite
123 crystallization was higher for La than Nd, and that overall apatite composition depended on the
124 RE cation present [36].

125 According to a study conducted on elucidating the effect of the RE identity and heat
126 treatment protocol on the oxyapatite crystallization in a Mo-free Na-Ca aluminoborosilicate glass
127 [37], crystallization behavior of glasses depends on the ionic radii of the rare-earth cation, where
128 the smaller the size of the rare-earth cation, the more sluggish is the tendency towards
129 crystallization. This effect was most pronounced for the smallest sized RE^{3+} ions (Lu^{3+} , Yb^{3+} ,
130 Er^{3+} , Y^{3+}), where no crystals were seen on slow cooling of the melt, a minor amount of
131 crystallization was viewable in monolithic samples (under an electron microscope) when heated
132 from room temperature, and crystals in amounts detectable by XRD were obtained only in glass-
133 ceramics produced through nucleation and crystallization in glass powders. Similar results have
134 also been reported by Goel et al. [38] for rare-earth containing alkaline-earth aluminoborosilicate
135 glass-ceramics. All oxyapatites large enough to be measured by EPMA were Ca-RE oxyapatites,
136 with mostly the target RE with a minor amount of Nd (included in all samples to facilitate optical
137 absorption measurements). . Of the four RE cations investigated in the study [37], glasses
138 containing Y^{3+} and Er^{3+} showed crystallization of oxyapatite and an unidentified RE “phase P,”
139 while the compositions containing Yb^{3+} and Lu^{3+} showed only the unidentified RE containing

140 phase and no oxyapatite. The authors [37] postulated that the RE in Ca-RE apatite must be close
141 to the size of the Ca^{2+} ion (in CN=9 “4f” or CN=7 “6h” sites in oxyapatite) in order to favor
142 crystallization, which suggests that smaller 3+ cations (Y, Er, Yb, Lu) may not favorably
143 incorporate into the oxyapatite lattice.

144 This article builds on the aforementioned work, and focuses on the effect of RE cation on
145 aluminoborosilicate glasses containing MoO_3 , both from a structural point of view in the
146 quenched glasses and the effects on crystallization upon slow cooling as would be experienced in
147 the glass-ceramic process. Understanding the partitioning of alkali cations towards Mo and RE
148 oxyanions are important considerations for minimizing the formation of poorly durable alkali
149 molybdate crystalline phases. The current study aims to assess the effect of RE cation size on the
150 partitioning of RE ion to molybdate and apatite phases and to ascertain the partitioning of alkali,
151 alkaline earth, and RE ions near molybdate oxyanions.

152

153 **2 Experimental methods**

154 **2.1 Synthesis**

155 **2.1.1 Quenched method synthesis**

156 A simplified nuclear waste glass-ceramic composition comprising 12.14 Na_2O – 13.58
157 CaO – 3.15 ZrO_2 – 3.53 MoO_3 – 5.14 Al_2O_3 – 11.95 B_2O_3 – 50.51 SiO_2 (mol%) was chosen as
158 the baseline for this work. The baseline composition above has been derived from the more
159 complex GC-Mo 5.86 glass-ceramic composition being considered for immobilization of a waste
160 stream derived from aqueous reprocessing of UNF [6]. The simplification has been made
161 assuming Na_2O represents the total fraction of alkali oxides ($\text{Na}_2\text{O}+\text{Li}_2\text{O}+\text{Cs}_2\text{O}$), CaO represents
162 the alkaline-earth oxides ($\text{CaO}+\text{BaO}+\text{SrO}$), and each RE in the studied series of glasses
163 represents the total rare-earth oxides ($\text{Y}_2\text{O}_3 + \text{La}_2\text{O}_3 + \text{Ce}_2\text{O}_3 + \text{Pr}_2\text{O}_3 + \text{Nd}_2\text{O}_3 + \text{Sm}_2\text{O}_3 + \text{Eu}_2\text{O}_3 +$

164 Gd₂O₃) in the nuclear waste glass-ceramic, on a molar basis. In this work, a series of glasses
165 have been made with varying RE element (RE = La, Ce, Nd, Sm, Er, Yb) with nominal
166 composition 11.54 Na₂O – 12.91 CaO – 2.99 ZrO₂ – 3.36 MoO₃ – 4.93 RE₂O₃ – 4.89 Al₂O₃ –
167 11.36 B₂O₃ – 48.02 SiO₂ (mol%). These particular RE were chosen due to their prevalence as
168 fission products (La, Ce, Nd, Sm), their possible multivalent nature (Ce), and their small size for
169 contrast (Er, Yb). Additionally, most of the RE have accessible absorption or luminescent
170 transitions for investigating local site symmetry in future studies. Sample names reflect the RE
171 used, i.e., CeNaCaMo, where the Ce glass was batched using CeO₂ precursor but assuming
172 Ce₂O₃ stoichiometry for the batch calculations.

173 To see the partitioning of alkali and alkaline earth cations towards Mo and/or RE
174 oxyanions, a second series of samples was also synthesized, where certain components have
175 been individually normalized out, such as RE₂O₃, Na₂O + CaO, or MoO₃. The only exception to
176 this formulation is one glass where Na₂O was removed, and an equal molar concentration of CaO
177 was added (i.e., LaCaMo). In this series of glasses, La was used as the RE. In each case the
178 component removed is represented by removing the element from the sample name, e.g.,
179 NaCaMo (La₂O₃ removed), LaCaMo (Na₂O removed), LaMo (Na₂O and CaO removed),
180 LaNaCa (MoO₃ removed). Since Al₂O₃, B₂O₃, SiO₂, and ZrO₂ are in all compositions, they are
181 not included in the sample name. [Table 1](#) summarizes the batched compositions of oxides of the
182 glasses being investigated in the present study, in mol% (mass% values are provided in
183 [Supplementary Information, Table S-1](#)).

184 All glasses were prepared by melt quenching. Homogeneous mixture of batches
185 corresponding to 20 g oxides (in accordance with compositions presented in [Table 1](#)) were made
186 using the following precursors; Al₂O₃ (Fisher Chemicals), H₃BO₃ 99% (Fisher Bioreagents),

187 CaCO₃ 99% (Fisher chemicals), Na₂CO₃ 99.5% (Fisher Chemicals), SiO₂ 98.6% (MIN-U-
188 SIL®10), ZrO₂ 99+% (STREM Chemicals), MoO₃ 99.5% (Alfa Aesar), and RE₂O₃ [La₂O₃
189 99.99% (Acros Organics), Nd₂O₃ 99.9% (Alfa Aesar) Sm₂O₃ 99.99% (Alfa Aesar), Er₂O₃ 99.9%
190 (Alfa Aesar), Yb₂O₃ 99.9% (Alfa Aesar), CeO₂ 99.9% (Acros Organics)]. The batches were
191 melted in a 90% Pt – 10% Rh crucible at 1300 °C for 2 h followed by quenching the crucible in
192 water at room temperature. The LaMo sample had a higher melting temperature in comparison to
193 other batches. Therefore it was melted at 1600 °C for only 15 min, to avoid the elevated loss of
194 volatile components. The as-synthesized samples were crushed to powder using a tungsten
195 carbide mill and re-melted under the same conditions to ensure homogenization. The re-melt
196 temperature was limited to 1300 °C (including LaMo sample) in order to decrease the volatility
197 and to emulate the targeted operating temperature (~1350 °C) of the cold crucible induction
198 melter (CCIM), in which these glasses would ultimately be melted for making nuclear waste
199 glass-ceramics [6]. After the second melt, the samples inside crucibles were again quenched in
200 water then annealed near their glass transition temperature (i.e., T_g – 20 °C), as determined by
201 thermal analysis to remove any effects of stress. Portions of the glasses were crushed into
202 powder (particle size <125 μm) for x-ray diffraction (XRD) and Raman spectroscopy
203 measurements. It is noteworthy that though the compositional analysis of the as-melted samples
204 was not performed, minimal change in the batched versus melted composition is expected, based
205 on results obtained in our recent study where negligible volatilization was observed from glass
206 melts of similar compositions melted at 1400 – 1500 °C [11].

207 2.1.2 Slow Cool Heat Treatment

208 To understand the crystallization behavior for the proposed glass-ceramic waste form, a
209 heat treatment similar to the 1× canister centerline cooling (CCC) profile, given in Crum et al.

210 [6] was used, as shown in Table S-2. To perform the slow cooling experiment, twice melted and
211 quenched samples were crushed to powder and loaded again in a 90% Pt – 10% Rh boat and
212 heated at 10 °C/min to 1300 °C, held for 1 h to ensure melt homogeneity, and then cooled
213 according to the profile given in Table S-2. At 400 °C, (temperature below the glass transition),
214 samples were taken out from the furnace and cooled in air to room temperature. The slowly
215 cooled samples were labeled -X after the corresponding quenched sample name (e.g.,
216 ErNaCaMo-X). For characterization purposes, the obtained samples were partly crushed to
217 powder and partly polished in parallel slabs.

218 2.2 Characterization

219 Glasses and glass-ceramics were characterized using X-ray diffraction (XRD) with a
220 PANalytical X'Pert Pro using a Cu K_{α} (1.541874 Å) line with the tube at 45 kV and 40 mA. The
221 data were collected in the 2θ range of 10 – 90° with a step size of 0.05° and dwell of 0.10 s at
222 each step. Six scans were obtained for each sample, and the analyses were performed on the
223 summed results. For quantitative phase analysis purposes, 10 mass% corundum Al₂O₃ (Fisher
224 Chemicals) was added as an internal standard, and quantitative phase analysis was performed
225 using Rietveld refinement and Highscore 4.5 or Topas software. Refinement comparison
226 between two software packages and two operators suggested an estimated fitting error of ~5%
227 (of the baseline value) on the total amorphous fraction, while a larger error of 1/4 – 2/5 of the
228 crystal fraction value on the individual crystalline phases, which ranged from 2 – 20 mass%
229 abundant.

230 Raman spectra were obtained by using a Renishaw InVia Raman microscope with a 632
231 nm (red) laser excitation source with acquisition time of 10 sec, and three repeated spectra being
232 summed. To confirm homogeneity, data were collected at multiple points.

233 Mo K-edge X-ray absorption spectroscopy (XAS) was performed in transmission mode
234 on beam line BL-27 at the PF Ring at the Photon Factory synchrotron facility (Tsukuba, Japan).
235 The PF Ring operates at 2.5 GeV with a 300 mA ring current. Beamline experiment details are
236 provided in the Supplementary Information. Spectra were recorded between 19800 and 21060
237 eV with energy steps of 2 eV (19800 – 19960), 0.5 eV (19960 – 20060), 2 eV (20060 – 20460),
238 and 4 eV (20460 – 21060). An accumulation time of 1 s step⁻¹ was used for all regions. For
239 each sample six spectra were averaged to improve the signal to noise ratio. Spectra were
240 recorded for five glasses and six crystalline standards. The crystalline standards used were:
241 MoO₂ (Sigma Aldrich) containing Mo⁴⁺ in octahedral coordination, MoO₃ (Sigma Aldrich)
242 containing Mo⁶⁺ in octahedral coordination, Na₂MoO₄ and three molybdates (CaMoO₄,
243 SrMoO₄, BaMoO₄) which were all synthesized in-house [39] and contain Mo⁶⁺ in tetrahedral
244 coordination. All standards were confirmed to be phase pure by X-ray diffraction. Samples for
245 XAS were dispersed in PEG with ratios optimized to achieve approximately one absorption
246 length thickness while maintaining a suitable Mo K absorption edge. Data reduction and
247 subsequent analysis was performed using the Demeter suite of programmes (Athena, Artemis,
248 and Hephaestus) [40], where analysis of X-ray Absorption Near Edge Structure (XANES) and
249 Extended X-ray Absorption Fine Structure (EXAFS) analysis were performed, details in the
250 Supplementary Information.

251 To observe the phase separation, as well as crystalline structure present (if any) in both
252 quenched and heat treated samples, the samples were further analyzed by electron probe
253 microanalysis (EPMA) using a JEOL JXA-8500F field emission electron microprobe equipped
254 with five wavelength-dispersive X-ray spectrometers (WDS). Analytical conditions, counting
255 times, and calibration standards for quantitative WDS analyses may be found in Supplementary

256 [Table S-3](#). Back-scattered electron (BSE) images and qualitative energy dispersive X-ray spectra
257 (EDS) were also collected using the same electron microprobe.

258

259 **3 Results and Discussion**

260 **3.1 Quenched glasses**

261 **3.1.1 Visible observation**

262 As shown in [Fig. S-1](#), all the glasses with 4.93 mol.% (~20 mass%) of RE₂O₃, except
263 CeNaCaMo, were transparent despite containing 3.36 mol.% (~6 mass%) MoO₃. The same
264 composition with RE₂O₃ normalized out (i.e., NaCaMo) was opaque, indicating the importance
265 of RE for enhancing Mo solubility as has been observed by other authors, e.g. [11].

266 For the CeNaCaMo sample, phase separation in the glass was evident, ([Fig. S-1](#) lower
267 image, showing top and bottom/quench side), and a yellowish phase was noted on the surface
268 which was in contact with the crucible bottom. A brown-colored glassy matrix was present on
269 the top side of this glass. The coloration of Ce-doped borosilicate glasses has been described
270 [41], indicating that 100% Ce³⁺ in a borosilicate glass matrix is hard to achieve, and there is
271 always some Ce⁴⁺ still present. In general, the color of a Ce-doped borosilicate glass changes
272 from yellow to brown with latter being a characteristic of 4+ oxidation state being dominant.
273 Therefore, the brown-colored glasses observed in the current study indicate a high concentration
274 of Ce in the 4+ state. However, that does not negate the presence of Ce³⁺ in these glasses as it is
275 known from the literature that Ce is always present in both valence states (3+ and 4+) in
276 borosilicate glasses [41-43]. Most other REs, including the other REs in the current study, should
277 only be present in the +3 state in a borosilicate glass [44].

278 In the second series of glasses, where single components were removed, glasses were
279 white and opaque, except LaNaCa where MoO₃ was removed from the composition ([Fig. S-1](#)).

280 This result suggests that the MoO_3 may be responsible for the opacity in the other samples, i.e.,
281 NaCaMo (RE_2O_3 removed), LaCaMo (Na_2O removed), and LaMo (Na_2O and CaO removed).
282 Note that two phases were macroscopically evident in LaCaMo even after re-melt: (i) an opaque
283 white phase and, (ii) a thin transparent layer. The observed opacity is due to light scattering,
284 from either crystalline phases or amorphous phase separation, which was further determined by
285 XRD and microscopy (see below).

286 3.1.2 SEM and EDS analysis

287 To ensure homogeneity of the quenched samples as well as to observe phase separation
288 and/or crystalline phases present (if any), samples were analyzed by SEM with BSE images.
289 Also, to check for any volatile element loss, a semi-quantitative EDS point analysis was
290 performed done on a minimum of three different arbitrary spots. The obtained SEM images are
291 shown in [Fig. S-3](#). SEM analyses were consistent with the XRD results, in that crystalline phases
292 were observed in NaCaMo and 493Ce samples. All other samples appeared chemically
293 homogeneous. Even in the cases of LaCaMo and LaMo, despite being visibly opaque and having
294 minor SEM-BSE color contrast, EDS showed nearly identical chemical compositions in all spots.
295 The color contrast was possibly from B-enriched and B-poor phases which could not be detected
296 from EDS. Further discussion is provided in the [Supplementary Information](#).

297 3.1.3 XRD analysis

298 All quenched samples in both series were X-ray amorphous (see [Fig. 1](#)), except
299 CeNaCaMo from series 1 and NaCaMo from series 2. It was notable that LaCaMo and LaMo
300 from series 2 were visibly opaque yet amorphous by XRD, indicating either a small fraction of
301 crystals below the detection limit of XRD or amorphous phase separation. In the case of the
302 other opaque samples, crystallization appeared to be the cause. The NaCaMo XRD showed

303 powellite (CaMoO_4) crystals, and the CeNaCaMo XRD showed Zr-doped ceria ($\text{Ce}_{0.9}\text{Zr}_{0.1}\text{O}_2$)
304 crystals.

305 To see the influence of re-melting (used to aid homogenization), quantification was
306 performed both after initial melting and after re-melting. In all cases, the fraction of crystalline
307 phases decreased after re-melting. Notably, ceria in the CeNaCaMo sample reduced from ~4.4
308 mass% to 3.1 mass%. XRD analysis of the LaMo sample after the first melting showed 1.08
309 mass% of zircon (ZrSiO_4) and ~0.12 mass% of quartz (SiO_2), but no crystals were observed after
310 the re-melting. The disappearance of crystal peaks in LaMo sample after re-melting did not,
311 however, produce a transparent sample.

312 3.1.4 Raman Analysis

313 Raman spectroscopy was performed to help in understanding the local structure of
314 borosilicate glass, particularly the local vibrational environment of Mo [45]. Raman spectra of all
315 quenched samples after re-melting (Fig. 2) were consistent with the literature data on similar
316 compositions [10, 25, 46]. The main characteristic bands of powellite (Raman spectrum of pure
317 synthetic CaMoO_4 added in Fig. 2) at 879, 848, 796, 393 and 322 cm^{-1} exactly matched the
318 bands observed in NaCaMo, indicating good agreement with the XRD results. These five
319 vibrational modes corresponded to the modes of the MoO_4^{2-} tetrahedron [25]. The peak at 879
320 cm^{-1} , corresponding to the symmetric stretch of the Mo-O bonds in MoO_4^{2-} tetrahedra, was the
321 most intense and characteristic peak for CaMoO_4 observed in the glasses and glass-ceramics
322 [45]. NaCaMo contained both Na and Ca, and therefore could theoretically form their respective
323 molybdates (Na_2MoO_4 and CaMoO_4). However, Mo crystallizes preferentially with Ca in this
324 system, as indicated by the absence of the characteristic band at 891 cm^{-1} for Na_2MoO_4 . The
325 likelihood of formation of Na_2MoO_4 versus CaMoO_4 depends upon relative concentrations of

326 various glass components, such as Na₂O, CaO, B₂O₃, and Al₂O₃, as described in the literature
327 [10, 14].

328 In the case of RE containing samples, the most intense peak was found to be at 914 cm⁻¹
329 or higher wavenumbers. The band at 914 cm⁻¹ or higher wavenumbers was also assigned to
330 MoO₄²⁻ tetrahedra symmetric stretching, with the shift of original band from 879 cm⁻¹ to 914
331 cm⁻¹ or higher wavenumbers due to the partial replacement of Ca²⁺ by RE³⁺ as the nearest
332 neighbor. It is known from the literature that REs can act as modifiers and compete for non-
333 bridging oxygen (NBO) with monovalent Na⁺ and bivalent Ca²⁺ [37, 47, 48]. A Raman band at
334 ~919 cm⁻¹ has been observed in a simplified SiO₂-CaO glass, containing a total of <1 mol%
335 Nd₂O₃ plus MoO₃, presumably due to isolated MoO₄²⁻ with nearby Ca²⁺ [49] or available Nd³⁺
336 located in close proximity to the MoO₄²⁻. This effect of the RE³⁺ ion on the molybdate oxyanion
337 stretch is further confirmed by the LaMo spectrum. Due to the absence of charge balancing Na⁺
338 and Ca²⁺ cations, La³⁺ cations play the role of charge balancing and occupy all the NBO places,
339 resulting in the characteristic Raman band appearing at even higher wavenumber, 932 cm⁻¹. The
340 origin of this 914 cm⁻¹ band from a Ca²⁺/RE³⁺- influenced molybdate ion was further confirmed
341 by the absence of this peak in the LaNaCa sample.

342 Additionally, there is a hump or shoulder at ~879 cm⁻¹ which can be observed especially
343 in LaNaCaMo, CeNaCaMo, NdNaCaMo and SmNaCaMo samples, which could be due to partial
344 phase separation of powellite crystals (not detected in XRD) or amorphous-like CaMoO₄, with
345 the latter being more likely due to the broad nature of the peak. Alternatively, this lower
346 frequency feature could be due to the antisymmetric stretch of molybdate (ν₃), which is ~60 cm⁻¹
347 lower than the symmetric stretch (ν₁) in molybdate with water ligands [50]. One final possibility
348 is that this mode is due to symmetric stretch of a different Mo-O distance or a slightly different

349 environment, as exemplified by the different vibrational modes expected for Mo-O of different
350 MoO_4^{2-} sites in $\text{Gd}_2(\text{MoO}_4)_3$, ranging from 959 to 851 cm^{-1} [45]. Even as charge density varies
351 for each RE, the Mo-O stretching frequency of 914 cm^{-1} is similar for RE ions close in size to
352 Ca^{2+} (La^{3+} , Ce^{3+} , Nd^{3+} and Sm^{3+}), whereas for smaller RE ions (Er^{3+} and Yb^{3+}) the band shifts to
353 922 cm^{-1} , confirming the different local environment around Mo for these smaller RE ions. This
354 shift of Mo-O stretching frequency is due to stronger coupling between MoO_4^{2-} and small RE^{3+}
355 ions, i.e., more Ca^{2+} cations replaced by smaller RE^{3+} ions (Er^{3+} and Yb^{3+}) (see Supplemental
356 Information for more discussion).

357 In the case of CeNaCaMo, as can be seen from Fig. 2, the most intense band is at 467 cm^{-1}
358 ¹, which is due to the F_{2g} vibrations of the cubic CeO_2 or $\text{Ce}_{0.9}\text{Zr}_{0.1}\text{O}_2$ [44, 51], and consistent
359 with the XRD results. In addition, there were also other features similar to those found in the
360 other RE-containing glasses, such as a band at 914 cm^{-1} , suggesting that some Ce^{3+} in the glass
361 was participating as a charge compensator around the molybdate. The remaining Ce formed a
362 ceria-rich layer on the bottom surface of the quenched glass (see Fig. S-1). This observation of
363 Ce in dual oxidation state is consistent with the EELS (electron energy loss spectroscopy) study
364 of Ce-doped borosilicate glasses, where it has been observed that the Ce in glassy phase adopts
365 primarily +3 state and the remaining Ce adopts +4 state as CeO_2 nanocrystal phase separated
366 from the glass [41, 52].

367 While considering the effect of alkali, it is useful to compare of spectra of LaNaCaMo
368 (which includes both Na and Ca) with LaCaMo (only Ca) and LaMo (no Na or Ca). In the LaMo
369 sample, the molybdate band shifts to the highest wavenumber observed (932 cm^{-1}), which can be
370 understood as La^{3+} cation acting as a charge compensator around MoO_4^{2-} due to the absence of
371 Na^+ or Ca^{2+} cations. In the case of LaCaMo, Ca^{2+} or La^{3+} will perform this charge compensator

372 role for molybdate, and for any other species such as on AlO_4^- and BO_4^- . From Fig. S-3, the
373 mean charge density of LaCaMo is slightly lower than that of LaMo. Therefore, a slightly lower
374 Mo-O shift was expected for LaCaMo than LaMo, and for LaCaMo the band at 924 cm^{-1} . This
375 confirmed the association of both La^{3+} and Ca^{2+} surrounding MoO_4^{2-} as a charge compensator.
376 For all studied samples, molybdate asymmetric and symmetric stretching lies in the range of 810
377 $- 840\text{ cm}^{-1}$ and $880 - 930\text{ cm}^{-1}$, respectively, strongly suggesting that Mo is in the 6+ state in
378 tetrahedral coordination. The octahedral Mo stretching bands of Mo-O terminal bond give
379 Raman vibrations in the range of $960\text{ cm}^{-1} - 1000\text{ cm}^{-1}$ [46].

380 The above results support either of the currently debated structural models about the
381 incorporation of molybdate ions in the glass structure. In the model proposed by Chouard et al.
382 [22], MoO_4^{2-} and RE^{3+} are found near to each other in the depolymerized zone. Alternatively, in
383 the model proposed by Bréhault et al. [11], MoO_4^{2-} and RE^{3+} are found near each other in a RE-
384 Mo-borate glassy phase. The Raman spectra can only show that MoO_4^{2-} and RE^{3+} are proximal,
385 not whether they are in a silicate, borate, or mixed borosilicate environment. The above results
386 did provide insight into the mechanism of Mo solubility enhancement in the presence of RE^{3+}
387 cations. Since Ca^{2+} cations were replaced by RE^{3+} around MoO_4^{2-} , the MoO_4^{2-} tetrahedral
388 species became more compact, which reduced the possibility of clustering of Mo-O-Mo and (Ca,
389 Na_2) MoO_4 formation. Also, due to the trivalent nature of RE^{3+} , it cross-polymerized the
390 borosilicate network, compensating multiple NBOs. This may explain why, even though RE^{3+}
391 and/or Ca^{2+} surrounded MoO_4^{2-} , no rare earth - molybdate crystalline phase (i.e., REMoO_4
392 and/or $\text{RE}_x\text{Ca}_{1-x}\text{MoO}_4$) or phase separation was observed in any of the quenched RE-containing
393 samples.

394 3.1.5 X-ray Absorption Spectroscopy

395 The Mo XANES spectra for the glasses and the standards are shown in Fig. 3a. There are
396 distinct changes in the spectra as a function of both oxidation state and local coordination
397 environment. To minimize the interference between the pre-edge and edge, the edge position
398 was defined as the energy where the edge jump is equal to 0.8 and there is a pseudo-linear
399 variation between the edge position and the oxidation state as shown in Fig. 3b. There is a small
400 spread of edge position for the $[\text{MoO}_4]^{2-}$ (molybdate)-containing reference compounds which is
401 related to residual interference effects from slight differences in the features on the low energy
402 side of the absorption edge and also in the XANES region after the edge. These are related to
403 subtle changes in the local structural environment of the Mo in the reference compounds. The
404 measured position of the absorption edges for the glass samples are given in Table 2; all the
405 values fall within those given for the suite of molybdate reference compounds. The presence of
406 the pre-edge feature in the glass samples is a clear signature of $[\text{MoO}_4]^{2-}$ molybdate moieties and
407 consistent with the measured absorption edge position (see Supplementary Information).

408 In order to investigate the local coordination environment of the Mo in the glass samples
409 the EXAFS region of the spectra were analyzed. The amplitude reduction factor (S_0^2) was
410 therefore determined from fitting the EXAFS data acquired for CaMoO_4 using the structural
411 model reported by Hazen et al. [53]. The $k^2 X(k)$ and the RDF for CaMoO_4 are shown in Fig. S-4
412 and the fit results are given in Table S-3. The nearest-neighbour Mo-O contribution at
413 approximately 1.35 Å (corresponding to an actual distance of 1.78 once phase shift effects have
414 been taken into account) dominates the RDF although weaker features between 2 and 4 Å are
415 related to contributions from other Mo-O, Mo-Ca, and Mo-Mo correlations. The refined value
416 for the nearest-neighbour (Mo-O) contact distance ($1.78 \text{ \AA} \pm 0.01$) was consistent with the

417 structural information and fitted values reported by Farges et al. [54], McKeown et al. [19], and
418 Short et al. [23].

419 The $k^2 X(k)$ and the RDF data for the glass samples are shown in Fig. 4 overlaid with the
420 data from the standards. The $k^2 X(k)$ consists of a unique damped sine function whose intensity
421 decreases with increasing k value. This is consistent with the sample being amorphous in
422 character and lacking any long range order beyond the first nearest-neighbour coordination shell.
423 No significant contributions can be seen beyond the first peak in the RDF indicating the Mo
424 atoms are not connected to the borosilicate glass network. From visual inspection it is clear that
425 the molybdenum environments in the glasses are similar to the $[\text{MoO}_4]^{2-}$ tetrahedral units in
426 CaMoO_4 . The glass data were fit with a model consisting of a single nearest-neighbour Mo-O
427 contribution and R , σ^2 , and ΔE were allowed to vary while S_o^2 was fixed at 0.73. The fitting
428 results are shown in Table 3 and for all the glasses the refined Mo-O distances are all statistically
429 equivalent to the tetrahedral Mo-O distance in CaMoO_4 . The fitted $k^2 X(k)$ and the corresponding
430 RDF for LaNaCaMo are shown in Fig. 5 as an example of the quality of the fits for the glass
431 samples. The coordination numbers for the LaNaCaMo, SmNaCaMo, and YbNaCaMo glasses
432 are all statistically equivalent to 4.0 which is also indicative of tetrahedral molybdate
433 environments. The refined coordination numbers for the LaCaMo and LaMo glasses are smaller
434 at 3.2 ± 0.4 and 2.9 ± 0.4 , respectively, though this difference from 4.0 may not be significant.
435 Attempts to incorporate contributions into the model from an additional Mo-O shell at a slightly
436 further distance proved unsuccessful even when the number of atoms in the shell was
437 constrained. Adjustment of the weighting of this path in increments of $N = 0.5$ resulted in a
438 progressive increase in the residual R-factor.

439 3.2 Heat-treated samples

440 As mentioned earlier, to understand the crystallization behavior in a canister, all samples
441 were slow cooled from the melt and further analyzed. Fig. S-2 shows selected samples after heat
442 treatment, all of which became opaque, as expected from crystallization and consequent light
443 scattering.

444 3.2.1 Electron Micrographs

445 Electron microscopy (backscattered electron, BSE, images) and microanalysis were used
446 to observe the microscopic structure of crystalline phases grown during slowly cooled heat
447 treatment of the samples. The obtained morphology of some selected samples is shown in Fig. 6.
448 Further images and an extended discussion are provided in Fig. S-7.

449 In general, powellite crystals were present in all RENaCaMo-X plus NaCaMo-X and
450 LaCaMo-X samples, generally in a cross-like structure. The only Mo-containing sample which
451 did not show powellite was LaMo, which on heat treatment showed multiple complex phase
452 separation. Powellites in this morphology have been observed in previous nuclear glass-ceramic
453 studies [6].

454 Oxyapatite crystals were observed for all RENaCaMo-X plus LaNaCa-X (Fig S-7a). In
455 YbNaCaMo-X, apatites were difficult to distinguish. No apatites could be seen in LaCaMo-X or
456 LaMo-X. Most oxyapatite crystals observed had skeletal morphology (like in [6]), while some of
457 them were arranged in flower-like structures with faceted morphology or tree/pyramidal
458 structures (similar to structures observed in [1, 55]). Needle-like oxyapatites are also seen,
459 depending on the orientation of the crystal, as seen in the literature [1, 4, 21, 37]. The presence of
460 multiple morphologies indicates that both short- and long-range diffusion or short-range and
461 melt-crystal interface mechanisms are responsible for this type of distribution and growth of

462 crystals [56]. Similar skeletal and pyramidal structures were observed in other glass-
463 crystallization studies with Nd and Mo-containing borosilicate glass-ceramics [6, 37].

464 Additionally, LaNaCaMo-X indicated that oxyapatite crystals were surface nucleated
465 whereas powellite crystals grew in the bulk matrix. This was confirmed by repeated polishing of
466 the samples and subsequent imaging (not shown), where it was observed that oxyapatite crystals
467 were removed with polishing whereas powellite crystals were still found in the matrix.

468 In the case of CeNaCaMo-X, ceria crystals were present (intense white phase) with
469 powellite as another phase (gray crosses similar to earlier images). Surprisingly, no apatite phase
470 was observed, though the small amount observed from XRD (see below) may have been
471 polished off during sample preparation.

472 In the case of YbNaCaMo-X, as observed from XRD, in addition to powellite and
473 oxyapatite crystalline phases, one additional phase is observed – keiviite ($\text{Yb}_2\text{Si}_2\text{O}_7$). Since the
474 elemental composition of both oxyapatite and keiviite are the same (Yb, Si, O), the contrast of
475 both phases in microprobe images are nearly same, so they are difficult to distinguish by this
476 means. However, from XRD analysis (see below), oxyapatite phase fraction is much smaller
477 compared to keiviite, so observed dendrite clusters (shown in [Fig. 6](#)) are likely keiviite. Probably
478 keiviite is the unidentified phase produced in Yb- and some Er-containing glass-ceramics
479 previously reported [37].

480 In LaCaMo-X, replacing Na^+ with Ca^{2+} shows a dramatic influence on heat treatment
481 behavior. Powellite still formed, mostly in chains with some crosses, but there is the formation of
482 an additional flower-like SiO_2 phase in the sample (dark phase in BSE image), which is
483 presumably amorphous according to XRD. It is significant to note that, even though Na^+ is not

484 needed in the typically observe Ca-RE oxyapatite phase, its absence in the glass composition
485 shows prevention of oxyapatite formation.

486 In the absence of both Na^+ and Ca^{2+} in LaMo-X, the main result of heat treatment was
487 multiple large-scale glass-in-glass phase separations. In this case, no powellite or oxyapatite
488 crystals were observed, but a small fraction of zircon was identified by XRD. These zircon
489 crystals can be seen in the micrographs as black spots inhomogeneously distributed in the matrix
490 producing a gray color (for more clarity, see [Fig. S-8d](#) mapping image with Zr distribution).
491 Another white/gray phase present was a B, Mo and La-rich amorphous phase, and the dark phase
492 was a Si-rich amorphous phase. This clearly showed the importance of Na^+ and/or Ca^{2+} for the
493 powellite and oxyapatite formation. The most significant aspect of this sample was the
494 identification of what appears to be a B-Mo-La amorphous phase (see [Fig. S-8d](#)) predicted in the
495 recently discussed theory of Bréhault et al. [11].

496 3.2.2 XRD phase analysis

497 All heat-treated glasses formed at least one crystalline phase, as seen from XRD patterns
498 ([Fig. 7](#)). The obtained crystalline phases and quantified relative amounts from Rietveld
499 refinement are shown in [Table 4](#). The actual Rietveld refinement fitting of each sample is shown
500 in [Fig. S-6](#). From the quantitative values of RENaCaMo-X, it was observed that a non-linear
501 trend in the amount of each phase was found moving smaller in RE ion size from LaNaCaMo-X
502 to YbNaCaMo-X. The amount of amorphous phase first increases up to NdNaCaMo-X and
503 subsequently decreases, while crystalline phases (i.e., powellite and oxyapatite) both decrease
504 then increase. There were small deviations in this trend due to additional crystal phases being
505 formed in CeNaCaMo-X (ceria) and YbNaCaMo-X (keiviite, $\text{Yb}_2\text{Si}_2\text{O}_7$) in addition to oxyapatite
506 and powellite.

507 Note that the oxyapatite phase obtained initially by the fitting software in each case is
508 somewhat different. In the LaNaCaMo-X, the oxyapatite selected as the best fit was $\text{La}_{8.9}\text{Si}_6\text{O}_{25.9}$,
509 which contained no Ca. Note that this phase was also formed in the LaNaCa-X glass. However,
510 after analysis of the microprobe data (see below) it was shown that Ca was invariably present in
511 apatite found. Therefore, all the apatites were analyzed as $\text{Ca}_2\text{RE}_8\text{Si}_6\text{O}_{26}$ for quantification,
512 where $\text{RE}=\text{La}^{3+}, \text{Ce}^{3+}, \text{Nd}^{3+}, \text{Sm}^{3+}, \text{Er}^{3+}, \text{or Yb}^{3+}$.

513 3.2.3 Raman analysis

514 The Raman spectra obtained after heat treatment complements the XRD data. As shown
515 in Fig. 8, in all samples except LaNaCa-X, CeNaCaMo-X and LaMo-X, characteristics peaks of
516 powellite (CaMoO_4) were seen, i.e., the symmetric Mo-O stretching band at 879 cm^{-1} and
517 asymmetric band at 847 cm^{-1} , 794 cm^{-1} , 393 cm^{-1} and 322 cm^{-1} . Despite the presence of
518 oxyapatite as shown in XRD results (Fig. 7 and Table 4), only powellite characteristics peaks
519 appeared in Raman spectra, except in the case of ErNaCaMo-X. This may be due to the lower
520 sensitivity of oxyapatite and higher sensitivity of powellite to the Raman exciting wavelength, so
521 due to the much higher intensity of powellite peaks, the oxyapatite peaks were suppressed.

522 In the case of ErNaCaMo-X, the appearance of oxyapatite peaks with powellite peaks
523 was due to the decrease of relative intensity of powellite peaks. The powellite characteristic
524 intense peak (i.e., the symmetric Mo-O stretching peak of MoO_4^{2-} tetrahedra at 879 cm^{-1}) in
525 ErNaCaMo-X appeared broader than powellite peaks in other samples (see Fig. 8). This
526 broadening may be due to disordered powellite crystals or additional amorphous CaMoO_4 . From
527 XRD results in Fig. 7, the presence of comparatively broadened peaks of CaMoO_4 confirms that
528 the CaMoO_4 crystals are very small, as seen in the electron micrographs.

529 In the case, where Mo was removed (LaNaCa-X) only oxyapatite peaks were found, and
530 when RE was removed (NaCaMo-X) only Raman peaks corresponding to powellite were found,
531 in agreement with XRD results. In LaNaCa-X Raman data, due to strong fluorescence (possibly
532 from Eu impurity), data above 1200 cm^{-1} has been removed to better view intensity of other
533 bands. In LaNaCa-X, the band at 856 cm^{-1} is due to symmetric stretching vibrations of Si-O
534 species. The lower wavenumber bands (706 cm^{-1} , 530 cm^{-1} and 402 cm^{-1}) are due to asymmetric
535 and bending vibration modes of Si-O. The stretching modes of La-O have been assigned in
536 literature at further lower wavenumber, i.e. between $268 - 280\text{ cm}^{-1}$ [57]. All the peaks of
537 LaNaCa-X were consistent and assigned according to the Guillot et al. [57] observations of
538 $\text{La}_{8.9}\text{Si}_6\text{O}_{25.9}$.

539 Similar to the CeNaCaMo sample before heat treatment, in CeNaCaMo-X the Raman
540 data showed an intense peak of ceria ($\text{Ce}_{0.9}\text{Zr}_{0.1}\text{O}_2$). Due to the very high intensity of the F_{2g}
541 vibration bands of the cubic ceria, all other characteristics peaks of other phases observed in
542 XRD (i.e., powellite and apatite) were not observed.

543 In LaCaMo Raman data in Fig. 2, the Mo-O vibration peak appeared at higher
544 wavenumber than RENaCaMo samples, so some differences in the heat treated sample were
545 expected. However, in LaCaMo-X the Raman behavior obtained was similar to RENaCaMo-X
546 samples in showing only powellite peaks.

547 In the case of LaMo-X, as expected from XRD analysis in Fig. 7, no powellite
548 characteristics peaks were observed. However, numerous new sharp bands at 1011 cm^{-1} , 976 cm^{-1} ,
549 440 cm^{-1} and 359 cm^{-1} were obtained, as shown in Fig. 8. Both 1011 cm^{-1} and 976 cm^{-1} were
550 assigned to $[\text{SiO}_4]^{4-}$ group stretching, the former to antisymmetric stretching with B_{1g} symmetry
551 (ν_3), and the latter to ν_1 stretching [58]. The bands at 440 cm^{-1} and 359 cm^{-1} were bending

552 modes ν_2 and ν_4 of the same $[\text{SiO}_4]^{4-}$ group. The bending mode vibrations peak intensity was
553 expected to be higher than stretching vibrations due to higher Si-O ionic character, as shown by
554 Dawson et al. [59]. In XRD, the crystal phase was identified as zircon (ZrSiO_4), which has been
555 observed in some other studies of similar compositions [60, 61]. The broad bands $\sim 927 \text{ cm}^{-1}$,
556 861 cm^{-1} , 708 cm^{-1} , 402 cm^{-1} were probably from different borate structures such as pentaborate
557 ($\sim 927 \text{ cm}^{-1}$) [62]. The borate was present in the remaining amorphous matrix, as shown in the
558 microscopy.

559 3.2.4 Quantitative EPMA analysis

560 To understand the exact chemical composition of each crystalline phase as well as the
561 overall distribution of certain elements in the matrix, all the samples were characterized by WDS
562 point analysis on the EPMA system. In several cases, EPMA mapping was also performed (see
563 Fig S-6). Quantitative analysis of crystal phases was determined in heat-treated glasses for
564 crystals in that were big enough to scan.

565 Powellite compositions were determined (Table 5) for NaCaMo-X, LaNaCaMo-X,
566 NdNaCaMo-X, and ErNaCaMo-X. Despite the fact that ErNaCaMo-X powellite crystals were
567 overall smaller in size, some crystals of $\sim 1 \mu\text{m}$ in size were found which were big enough for
568 spot analysis. An apparent trend was observed with RE^{3+} ion size, where La, Nd, and Er samples
569 progressively have less RE and Na and more Ca and Mo in them. This did not appear to be due
570 to interaction volume including surrounding glass but may be due to size and valence
571 compensation of the RE with Na. The sample with no RE (NaCaMo-X) appeared to have
572 essentially no Na, and a similar amount of Mo to the ErNaCaMo-X sample, though the total for
573 quantification was slightly low. By converting mass fractions of oxides into stoichiometry, the
574 measured powellites were (ignoring SiO_2 and Al_2O_3 , based on 4 atoms of O per formula unit)

575 approximately $\text{Ca}_{0.79}\text{Na}_{0.14}\text{La}_{0.11}\text{Mo}_{1.04}\text{O}_4$ (LaNaCaMo), $\text{Ca}_{0.88}\text{Na}_{0.08}\text{Nd}_{0.09}\text{Mo}_{1.03}\text{O}_4$
576 (NdNaCaMo), $\text{Ca}_{0.90}\text{Na}_{0.05}\text{Er}_{0.04}\text{Mo}_{1.02}\text{O}_4$ (ErNaCaMo), and $\text{Ca}_{0.96}\text{Mo}_{1.01}\text{O}_4$ (NaCaMo). Previous
577 EDS measurements of powellites in more complex glasses have shown substitution of alkali (Na,
578 Rb) and alkaline earth (Sr, Ba) [5, 6] and RE [10, 23-25]. This compositional change with RE
579 size was consistent with the fact that as RE^{3+} ion size decreases, the volume of the MoO_4^{2-}
580 tetrahedra decrease and become more isolated, hence it is easier for Ca^{2+} to interact with them to
581 form powellite during slow cooling. All these results were consistent with WDS compositional
582 maps shown in Fig S-8.

583 Oxyapatite phases were also measured (Table 6), for the RENaCaMo-X (RE=La, Nd,
584 Sm, Er). For the CeNaCaMo-X and YbNaCaMo-X, apatites were not found to be big enough to
585 measure reliably. The LaNaCa-X apatites were also measured, along with the YbNaCaMo-X
586 keiviite crystals.

587 For the quantification, apatite and keiviite in YbNaCaMo-X were difficult to distinguish
588 by electron imaging. Therefore, an average EPMA composition showed much higher SiO_2 and
589 lower CaO than other apatites likely from the greater contribution of the keiviite phase. Keiviite
590 crystals were very small and narrow, and interaction of the beam with the underlying glass is
591 likely, as suggested from the higher amounts of ZrO_2 and Al_2O_3 measured. For the keiviite
592 crystals, for pure stoichiometric $\text{Yb}_2\text{Si}_2\text{O}_7$ one would expect 76 mass% Yb_2O_3 and 24 mass%
593 SiO_2 ; clearly, from the analysis, the RE is far too low, and other elements are shown suggesting
594 that some Yb-oxyapatite and/or some residual glass was sampled as well, or that there is
595 considerable substitution in this phase.

596 The overall inclusion of non-typical oxyapatite elements is worth discussing. In no case
597 was MoO_3 observed in these apatites. The ZrO_2 content was small but measurable and probably

598 real, but could also be interaction with surrounding glass. Al₂O₃ and Na₂O contents were very
599 small or zero. Although quantification of low boron concentrations by EPMA is not entirely
600 reliable due to poor counting statistics from boron's low X-ray yield and the fluorescence of
601 boron in the WDS diffracting crystal [63], the EPMA data indicates that, qualitatively, some
602 small amounts of B₂O₃ (~1-5 mass%) are being incorporated into the oxyapatite phases. This is
603 not unexpected crystallographically [35] and is consistent with previous glass-ceramic studies
604 [64].

605 Assuming that boron would go on the Si site and Zr would go on the Ca/RE site and not
606 accounting for any excess or deficient oxygen, the approximate stoichiometries can be estimated
607 as: Ca_{2.8}La_{6.3}Zr_{0.1}Si_{5.2}B_{1.4}O₂₆ (LaNaCa), Ca_{2.8}La_{6.5}Zr_{0.1}Si_{5.2}B_{1.3}O₂₆ (LaNaCaMo),
608 Ca_{2.7}Nd_{6.7}Zr_{0.1}Si_{5.3}B_{1.1}O₂₆ (NdNaCaMo), and Ca_{2.8}Sm_{6.5}Zr_{0.2}Si_{5.3}B_{0.9}O₂₆ (SmNaCaMo); (apatites
609 for Er and Yb were small, and the compositions are questionable). Overall, Ca levels are higher
610 than the 2 moles assumed in the XRD quantification, but clearly Ca is present and not
611 completely vacant with only the RE participating with vacancies. This small composition
612 difference should not affect the XRD phase quantification. Thus the main oxyapatite constituent
613 concentrations do seem to vary slightly with RE ion size. As observed in [Table 6](#), the Si
614 concentration decreased with RE³⁺ ion size decrease (La, Nd, Sm, Er). This appears to correlate
615 with an increasing concentration of ZrO₂ observed in these samples with decreasing RE ion size.
616 These changes were small and may not be statistically significant, and the ZrO₂ could be a result
617 of interaction with underlying glass, but this could not be definitively determined.

618 Additionally, the unit cell size of refined oxyapatite and powellite phases was determined
619 from Rietveld analysis of the XRD data, and compared to the RE³⁺ radii (Shannon [65] crystal
620 radii for coordination number 8) in [Fig. 9](#). It can be seen that there is a general trend that with

621 increasing radius of the RE, the unit cell volume of the refined phase increases. It should be
622 noted here that it was possible, then, to predict the presence of RE in both these phases even if
623 the crystals themselves were too small or scarce for EPMA quantification, such as was the case
624 for Yb and Ce apatites and Yb, Sm, and Ce powellites. It is recognized that the coordination
625 number of the RE in apatite would likely be 7 or 9 due to the apatite crystal structure, but
626 coordination number 8 was chosen as representative, and the trends are the same. The analysis
627 for oxyapatite should be valid given that the total amount of RE present in the analyzed
628 oxyapatite phase was approximately the same (26 – 28 mol% for all but the Er and Yb samples).
629 and the main variable in lattice volume should come from the size difference or at least a proxy
630 for lattice strain in which other substitutions are made. For the powellites the situation is
631 somewhat more complicated, in that multiple concentrations are changing (RE, Mo, Na, Ca), but
632 at least qualitatively the RE cation size does appear to trend with the lattice volume.

633 **4 Conclusions**

634 This study revealed the complex influence of RE³⁺ ion size on crystallization behavior in
635 Mo- and RE-containing simulated nuclear waste glass-ceramics. A key factor contributing to the
636 solubility of MoO₃ in these glasses was the presence of RE³⁺ cations and the isolation of MoO₄²⁻
637 tetrahedra due to the high field strength of the RE. The slow-cooling from the melt of samples
638 missing alkali and/or alkaline earth cations (LaCaMo-X and LaMo-X), it was clear that both Na⁺
639 and Ca²⁺ cationic species were required for the formation of oxyapatite, even though Na is not
640 present in any significant quantity in the crystal. This is despite the fact that theoretically as well
641 as experimentally oxyapatite formation is possible without these cation species (~RE₁₀Si₆O₂₆),
642 such as in the case of La_{10-x}Vac_x(SiO₆)₄O_{2±δ}, where ‘Vac’ indicates cation vacancies [57, 64].

643 Several important conclusions can be made from the study of interactions between RE
644 and Mo in aluminoborosilicate systems with and without alkali and alkaline earths. From the
645 XRD results of samples before heat treatment, it is shown that even ~6 mass% of MoO₃ can be
646 dissolved in the presence of ~20 mass% of RE₂O₃ without powellite crystallization. A key factor
647 of solubility of MoO₃ in the presence of RE³⁺ cations is the isolation of MoO₄²⁻ tetrahedron due
648 to the high field strength of RE³⁺ cations, as confirmed by Raman analysis. RE³⁺ cationic size
649 has a non-linear influence of on crystallization behavior of the studied samples, probably due to a
650 threshold value of charge density of RE³⁺ cations (i.e., in the studied case for smaller cations Er³⁺
651 and Yb³⁺), after which the coupling interaction between borosilicate network and these (Er³⁺ and
652 Yb³⁺) cations behaves differently in the glassy matrix. The smallest RE studied, Yb, tends to
653 crystallize only a small amount of apatite but a large amount of the RE silicate keiviite.

654 Fundamental relationships between the Mo and RE in the glasses and glass-ceramics
655 have been clarified. In all studied glasses the tetrahedral nature of MoO₄²⁻ and its +6 state are
656 further confirmed from Raman and XAS analysis, and all REs studied in are in the +3 state,
657 except Ce which is present in both +3 and +4. RE cations are near Mo in the glass, with higher
658 field strength cations changing the vibrational frequency in samples with different sized RE and
659 those without Na⁺ and/or Ca²⁺. Additionally, some RE appears to partition to the Ca molybdate
660 powellite crystalline phases (Ca, RE, Na)MoO₄, with smaller RE substituting to a lesser extent,
661 Na content generally trending with RE in powellite, and Mo possibly being deficient when RE
662 contents are high.

663

664

665 **Acknowledgements**

666 This research is being performed using funding received from the U.S. Department of
667 Energy – Office of Nuclear Energy through the Nuclear Energy University Program under the
668 award DE-NE0008431. The authors would like to thank Antoine Bréhault, Muad Saleh, Prashant
669 Rajbhandari, and Russell J. Hand for helpful conversations and comments. Thanks to Jacob
670 Peterson and Brian Riley for providing the alkaline earth molybdates for XAS standards.

671 **References**

- 672 [1] N. Chouard, D. Caurant, O. Majérus, N. Guezi-Hasni, J.-L. Dussossoy, R. Baddour-Hadjean and
673 J.-P. Pereira-Ramos, *J. Alloys Compd.* 671 (2016) 84-99.
- 674 [2] D. Caurant, P. Loiseau, O. Majérus, V. Aubin-Chevaldonnet, I. Bardez and A. Quintas, *Glasses,
675 Glass-Ceramics and Ceramics for Immobilization of Highly Radioactive Nuclear Wastes*, Nova
676 Science Publishers, Inc., New York (2009).
- 677 [3] A. Quintas, D. Caurant, O. Majérus, P. Loiseau, T. Charpentier and J.-L. Dussossoy, *J. Alloys
678 Compd.* 714 (2017) 47-62.
- 679 [4] J. V. Crum, L. Turo, B. Riley, M. Tang and A. Kossoy, *J. Am. Ceram. Soc.* 95 (2012) 1297-1303.
- 680 [5] J. V. Crum, J. J. Neeway, B. J. Riley, Z. Zhu, M. J. Olszta and M. Tang, *J. Nucl. Mater.* 482
681 (2016) 1-11.
- 682 [6] J. Crum, V. Maio, J. McCloy, C. Scott, B. Riley, B. Benefiel, J. Vienna, K. Archibald, C.
683 Rodriguez, V. Rutledge, Z. Zhu, J. Ryan and M. Olszta, *J. Nucl. Mater.* 444 (2014) 481-492.
- 684 [7] O. Pinet, J. L. Dussossoy, C. David and C. Fillet, *J. Nucl. Mater.* 377 (2008) 307-312.
- 685 [8] J. McCloy and A. Goel, *MRS Bull.* 42 (2017) 233-240.
- 686 [9] Y. Kawamoto, K. Clemens and M. Tomozawa, *J. Am. Ceram. Soc.* 64 (1981) 292-296.
- 687 [10] D. Caurant, O. Majérus, E. Fadel, A. Quintas, C. Gervais, T. Charpentier and D. Neuville, *J.
688 Nucl. Mater.* 396 (2010) 94-101.
- 689 [11] A. Brehault, D. Patil, H. Kamat, R. E. Youngman, L. M. Thirion, J. C. Mauro, C. L. Corkhill, J.
690 S. McCloy and A. Goel, *J. Phys. Chem. B* 122 (2018) 1714-1729.
- 691 [12] G. Calas, M. Le Grand, L. Galois and D. Ghaleb, *J. Nucl. Mater.* 322 (2003) 15-20.
- 692 [13] N. Henry, P. Deniard, S. Jobic, R. Brec, C. Fillet, F. Bart, A. Grandjean and O. Pinet, *J. Non-
693 Cryst. Solids* 333 (2004) 199-205.
- 694 [14] D. Caurant, O. Majérus, E. Fadel, M. Lenoir, C. Gervais and O. Pinet, *J. Am. Ceram. Soc.* 90
695 (2007) 774-783.
- 696 [15] C. Martineau, V. K. Michaelis, S. Schuller and S. Kroecker, *Chem. Mater.* 22 (2010) 4896-4903.
- 697 [16] B. J. Greer and S. Kroecker, *Phys. Chem. Chem. Phys.* 14 (2012) 7375-7383.
- 698 [17] M. Magnin, S. Schuller, C. Mercier, J. Trébosc, D. Caurant, O. Majérus, F. Angéli and T.
699 Charpentier, *J. Am. Ceram. Soc.* 94 (2011) 4274-4282.
- 700 [18] N. C. Hyatt, R. J. Short, R. J. Hand, W. E. Lee, F. Livens, J. M. Charnock and R. L. Bilsborrow,
701 *The Structural Chemistry of Molybdenum in Model High Level Nuclear Waste Glasses,
702 Investigated by MO K-Edge X-Ray Absorption Spectroscopy. Environmental Issues and Waste
703 Management Technologies in the Ceramic and Nuclear Industries X*, John Wiley & Sons, Inc.
704 (2006).
- 705 [19] D. A. McKeown, H. Gan and I. L. Pegg, *J. Nucl. Mater.* 488 (2017) 143-149.
- 706 [20] K. Konstantinou, P. V. Sushko and D. M. Duffy, *Phys. Chem. Chem. Phys.* 18 (2016) 26125-
707 26132.
- 708 [21] N. Chouard, D. Caurant, O. Majérus, J. L. Dussossoy, S. Klimin, D. Pytalev, R. Baddour-Hadjean
709 and J. P. Pereira-Ramos, *J. Mater. Sci.* (2014) 1-23.

- 710 [22] N. Chouard, D. Caurant, O. Majérus, J. L. Dussossoy, A. Ledieu, S. Peugeot, R. Baddour-Hadjean
711 and J. P. Pereira-Ramos, *J. Non-Cryst. Solids* 357 (2011) 2752-2762.
- 712 [23] R. J. Short, R. J. Hand, N. C. Hyatt and G. Möbus, *J. Nucl. Mater.* 340 (2005) 179-186.
- 713 [24] T. Taurines and B. Boizot, *J. Non-Cryst. Solids* 357 (2011) 2723-2725.
- 714 [25] T. Taurines, D. Neff and B. Boizot, *J. Am. Ceram. Soc.* 96 (2013) 3001-3007.
- 715 [26] D. Bosbach, T. Rabung, F. Brandt and T. Fanghänel, *Radiochim. Acta* 92 (2004) 639-643.
- 716 [27] E. Kashchieva, I. Petrov, L. Aleksandrov, R. Iordanova and Y. Dimitriev, *Phys. Chem. Glasses*
717 53 (2012) 264-270.
- 718 [28] A. Kossoy, R. Schulze, M. Tang, D. J. Safarik and R. J. McCabe, *J. Nucl. Mater.* 437 (2013) 216-
719 221.
- 720 [29] D. Caurant, O. Majerus, P. Loiseau, I. Bardez, N. Baffier and J. L. Dussossoy, *J. Nucl. Mater.* 354
721 (2006) 143-162.
- 722 [30] A. Quintas, O. Majérus, D. Caurant, J.-L. Dussossoy and P. Vermaut, *J. Am. Ceram. Soc.* 90
723 (2007) 712-719.
- 724 [31] T. H. Le, N. R. Brooks, K. Binnemans, B. Blanpain, M. Guo and L. Van Meervelt, *Acta Cryst. E*
725 72 (2016) 209-211.
- 726 [32] N. Christensen, R. G. Hazell and A. W. Hewat, *Acta Chem. Scandan.* 51 (1997) 37-43.
- 727 [33] W. J. Weber, *Radiation Eff.* 77 (1983) 295-308.
- 728 [34] W. J. Weber and R. B. Gregor, *Nucl. Instr. Meth. B* 46 (1990) 160-164.
- 729 [35] J. Ito, *Amer. Mineral.* 53 (1968) 890-907.
- 730 [36] A. Kidari, J.-L. Dussossoy, E. Brackx, D. Caurant, M. Magnin and I. Bardez-Giboire, *J. Am.*
731 *Ceram. Soc.* 95 (2012) 2537-2544.
- 732 [37] A. Quintas, D. Caurant, O. Majerus, J. L. Dussossoy and T. Charpentier, *Phys. Chem. Glasses* 29
733 (2008) 192-197.
- 734 [38] A. Goel, A. A. Reddy, M. J. Pascual, L. Gremillard, A. Malchere and J. M. F. Ferreira, *J. Mater.*
735 *Chem.* 22 (2012) 10042-10054.
- 736 [39] J. A. Peterson, J. V. Crum, B. J. Riley, R. M. Asmussen and J. J. Neeway, *J. Nucl. Mater.* under
737 review (2018).
- 738 [40] B. Ravel and M. Newville, *J. Synchr. Rad.* 12 (2005) 537-541.
- 739 [41] M. Shiratori, Ultraviolet-absorbing glass tube for fluorescent lamp and glass tube comprising the
740 same for fluorescent lamp, USPTO, US 20090280277 A1 (2009).
- 741 [42] B. Yale and K. M. Fyles, Borosilicate glass compositions incorporating cerium oxide, USPTO,
742 US 5017521 A (1991).
- 743 [43] Z. Wang and L. A. Cheng, *Phys. Chem. Glasses* 55 (2014) 182-189.
- 744 [44] P. Sudarsanam, B. Mallesham, D. N. Durgasri and B. M. Reddy, *RSC Adv.* 4 (2014) 11322-
745 11330.
- 746 [45] F. D. Hardcastle and I. E. Wachs, *J. Raman Spectrosc.* 21 (1990) 683-691.
- 747 [46] L. Aleksandrov, T. Komatsu, R. Iordanova and Y. Dimitriev, *J. Phys. Chem. Solids* 72 (2011)
748 263-268.

- 749 [47] J. A. Johnson, C. J. Benmore, D. Holland, J. Du, B. Beuneu and A. Mekki, *J. Phys. Cond. Matt.*
750 23 (2011) 065404.
- 751 [48] M. Wilding, Y. Badyal and A. Navrotsky, *J. Non-Cryst. Solids* 353 (2007) 4792-4800.
- 752 [49] M. Magnin, S. Schuller, D. Caurant, O. Majérus, D. d. Ligny and C. Mercier, Effect of
753 Compositional Changes on the Structure and Crystallization Tendency of a Borosilicate Glass
754 Containing MoO₃. *Environmental Issues and Waste Management Technologies in the Materials*
755 *and Nuclear Industries XII*, John Wiley & Sons, Inc. (2009).
- 756 [50] N. Weinstock and H. Schulze, *J. Chem. Phys.* 59 (1973) 5063-5067.
- 757 [51] T. Taniguchi, T. Watanebe, S. Ichinohe, M. Yoshimura, K.-i. Katsumata, K. Okada and N.
758 Matsushita, *Nanoscale* 2 (2010) 1426-1428.
- 759 [52] G. Yang, R. Hand and G. Möbus, *J. Phys. Conf. Ser.* 126 (2008) 012021.
- 760 [53] R. M. Hazen, L. W. Finger and J. W. E. Mariathasan, 46 (1985) 253-263.
- 761 [54] F. Farges, R. Siewert, G. E. Brown, A. Guesdon and G. Morin, *Canad. Mineral.* 44 (2006) 731-
762 753.
- 763 [55] A. Quintas, D. Caurant, O. Majérus, T. Charpentier and J. L. Dussossoy, *Mat. Res. Bull.* 44
764 (2009) 1895-1898.
- 765 [56] R. J. Kirkpatrick, *Amer. Mineral.* 60 (1975) 798-814.
- 766 [57] S. Guillot, S. Beaudet-Savignat, S. Lambert, P. Roussel, G. Tricot, R.-N. Vannier and A.
767 Rubbens, *J. Raman Spectrosc.* 42 (2011) 1455-1461.
- 768 [58] A. Gucsik, M. Zhang, C. Koeberl, E. K. H. Salje, S. A. T. Redfern and J. M. Pruneda, *Mineral.*
769 *Mag.* 68 (2004) 801-811.
- 770 [59] P. Dawson, M. M. Hargreave and G. R. Wilkinson, *J. Phys. C Solid State Phys.* 4 (1971) 240.
- 771 [60] S. Schuller, O. Pinet, A. Grandjean and T. Blisson, *J. Non-Cryst. Solids* 354 (2008) 296-300.
- 772 [61] S. Schuller, O. Pinet and B. Penelon, *J. Am. Ceram. Soc.* 94 (2011) 447-454.
- 773 [62] G. Padmaja and P. Kistaiah, *J. Phys. Chem. A* 113 (2009) 2397-2404.
- 774 [63] J. J. McGee and L. M. Anovitz, Electron probe microanalysis of geologic materials for boron. In:
775 L. M. Anovitz and E. S. Grew, Editors, *Reviews in Mineralogy, Petrology and Geochemistry*,
776 Mineralogical Society of America, Chantilly, VA (1996).
- 777 [64] L. Li, D. M. Strachan, H. Li, L. L. Davis and M. Qian, *J. Non-Cryst. Solids* 272 (2000) 46-56.
- 778 [65] R. D. Shannon, *Acta Crystallog. A* 32 (1976) 751-767.
- 779

780 **Tables**781 **Table 1.** Chemical compositions of the target samples in mol%.

Sample Name	RE ₂ O ₃	Na ₂ O	CaO	MoO ₃	SiO ₂	B ₂ O ₃	Al ₂ O ₃	ZrO ₂
NaCaMo	-	12.14	13.58	3.53	50.51	11.95	5.14	3.15
LaNaCaMo	4.93	11.54	12.91	3.36	48.02	11.36	4.89	2.99
CeNaCaMo	4.93	11.54	12.91	3.36	48.02	11.36	4.89	2.99
NdNaCaMo	4.93	11.54	12.91	3.36	48.02	11.36	4.89	2.99
SmNaCaMo	4.93	11.54	12.91	3.36	48.02	11.36	4.89	2.99
ErNaCaMo	4.93	11.54	12.91	3.36	48.02	11.36	4.89	2.99
YbNaCaMo	4.93	11.54	12.91	3.36	48.02	11.36	4.89	2.99
LaCaMo	4.93	-	24.45	3.36	48.02	11.36	4.89	2.99
LaMo	6.53	-	-	4.45	63.56	15.04	6.47	3.96
LaNaCa	5.10	11.94	13.36	-	49.69	11.75	5.06	3.10

782

783 **Table 2.** Mo K-edge energy (defined as the energy where the edge jump is equal to 0.8) and
784 average oxidation state for reference standards and glass samples.

Sample name	K-edge energy (eV)	Mo Ox. state
Mo metal	20010.0	0
MoO ₂	20015.2	4
MoO ₃	20018.9	6
Na ₂ MoO ₄	20020.4	6
BaMoO ₄	20019.8	6
SrMoO ₄	20019.0	6
CaMoO ₄	20018.5	6
LaNaCaMo	20019.3	6
SmNaCaMo	20019.2	6
YbNaCaMo	20019.3	6
LaCaMo	20018.8	6
LaMo	20018.6	6

785

786

787 **Table 3.** Structural parameters for glass samples obtained from the Mo K-edge fits. $R_{\text{Mo-i}}$ is the
 788 average interatomic distance for a given pair (Mo-i) of atoms. σ_i^2 is the Debye-Waller factor
 789 (estimated from the distribution of bond lengths) and $N_{\text{Fe-i}}$ is the refined number of scattered in
 790 the coordination shell. The refined amplitude reduction factor (S_0^2) determined from fitting of the
 791 CaMoO_4 data was fixed at 0.73. The fit range in k space was from 1.75 to 15.5 \AA^{-1} and in R
 792 space from 1.0 to 6.0 \AA . The number of independent variables (N_v) and independent data points
 793 (N_{ip} , determined from the Nyquist theorem) was $N_v = 4$ and $N_{\text{ip}} = 43$, respectively.

Sample name	E_0 (eV)	\pm	$R_{\text{Mo-O1}}$ (\AA)	\pm	$N_{\text{Mo-O1}}$	\pm	σ^2 (\AA^2)	\pm	R-factor
LaNaCaMo	0.9	0.8	1.788	0.006	3.9	0.4	0.0013	0.0007	0.04
SmNaCaMo	0.0	0.8	1.791	0.006	3.7	0.4	0.0011	0.0007	0.04
YbNaCaMo	1.1	0.9	1.788	0.007	4.2	0.6	0.0023	0.0008	0.05
LaCaMo	-0.8	0.8	1.788	0.006	3.2	0.4	0.0011	0.0006	0.05
LaMo	-1.2	0.8	1.789	0.006	2.9	0.4	0.0014	0.0007	0.05

794

795

796 **Table 4.** The obtained crystalline phases and its quantitative values from XRD analysis.
 797 Estimated phase fraction errors are ~5% on the amorphous fraction and 1/4 to 2/5 of the stated
 798 value for the crystalline fractions.

Sample Name (-X)	Powellite/ CaMoO_4 (Mass %)	Oxyapatite/ $\text{Ca}_2\text{RE}_8\text{Si}_6\text{O}_{26}$ (Mass %)	Other (Mass %)	Amorphous (Mass %)
NaCaMo	4.6	-	-	95.4
LaNaCa		9.5		90.5
LaNaCaMo	5.3	13.4		81.3
CeNaCaMo	3.3	3.9	3.1 Ceria/ $\text{Ce}_{0.9}\text{Zr}_{0.1}\text{O}_2$	89.7
NdNaCaMo	5	10		85
SmNaCaMo	4.2	11.5		84.4
ErNaCaMo	3.9	13.1		83
YbNaCaMo	4.8	1.7	9.5 Keiviite/ $\text{Yb}_2\text{Si}_2\text{O}_7$	84
LaCaMo	2.6			97.4
LaMo			3 Zircon/ ZrSiO_4	97

799

800

801 **Table 5.** Quantitative analysis of powellite phases in different heat-treated samples from electron
 802 probe microanalysis (EPMA) in mass%. Values are an average of 2-3 individual measurements.
 803 Typical detection limits for each element are also reported. BDL = below detection limit, ND =
 804 not determined. Note that -X (heat treated) is not added to the names in the table but is implied.
 805 *Only one useable measurement of NaCaMo.

	LaNaCaMo		NdNaCaMo		ErNaCaMo		NaCaMo*		Detection Limit
	Avg	StdDev	Avg	StdDev	Avg	StdDev	Avg	StdDev	
MoO ₃	67.6	0.2	69.7	0.9	71.0	1.5	72.0	-	0.20
SiO ₂	0.56	0.39	0.29	0.12	0.30	0.06	0.37	-	0.04
ZrO ₂	BDL	BDL	BDL	BDL	0.17	0.13	0.00	-	0.13
B ₂ O ₃	ND	ND	ND	ND	ND	ND	ND	ND	ND
Al ₂ O ₃	1.02	0.32	BDL	BDL	1.02	0.21	0.60	-	0.04
CaO	20.1	0.5	23.1	0.8	24.4	0.5	26.7	-	0.02
Na ₂ O	1.97	0.35	1.11	0.07	0.82	0.48	BDL	BDL	0.06
RE ₂ O ₃	8.29	1.15	6.76	0.90	3.25	0.67	BDL	BDL	0.09
Total	99.5		101.0		100.9		99.8		

806

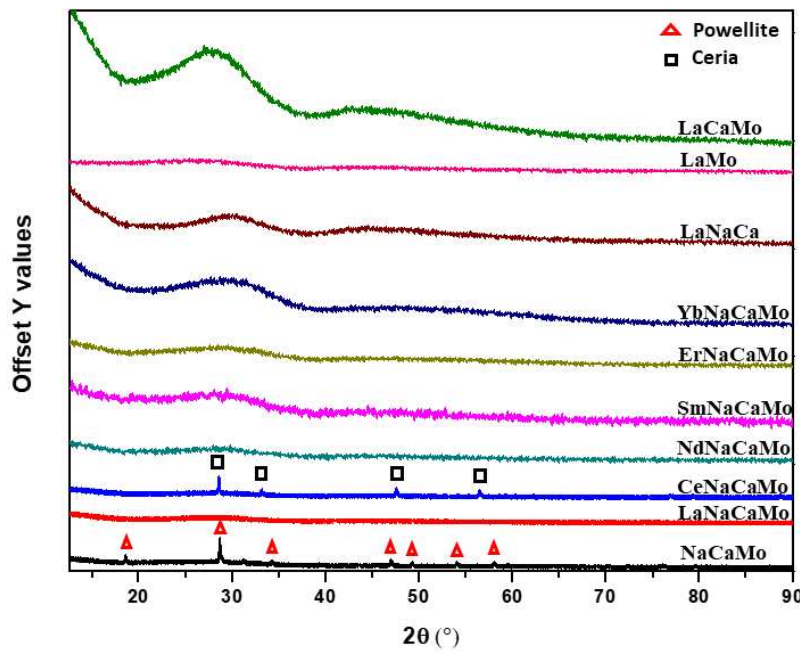
807

808 **Table 6.** Quantitative analysis of oxyapatite phases in different heat-treated samples from
 809 electron probe microanalysis (EPMA) in mass%. Note that, for YbNaCaMo-X, due to
 810 indistinguishable contrast and morphology, oxyapatite and keiviite phases were added and the
 811 total quantitative value averaged. Note that -X (heat treated) is not added to the names in the
 812 table but is implied. Values are an average of 7-14 individual measurements. Typical detection
 813 limits for each element are also reported. BDL = below detection limit.

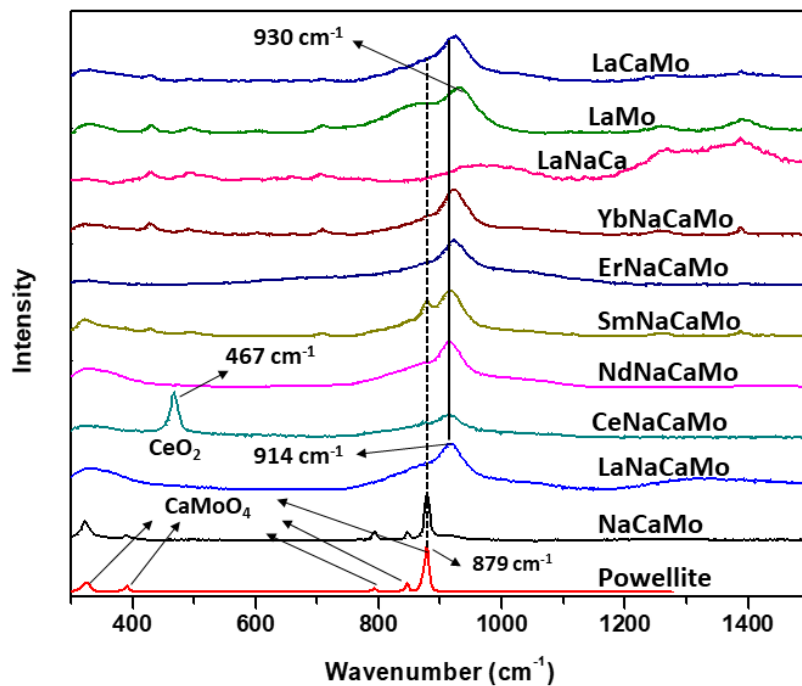
	LaNaCa		LaNaCaMo		NdNaCaMo		SmNaCaMo		ErNaCaMo		YbNaCaMo		Detection Limit
	Avg	StdDev	Avg	StdDev	Avg	StdDev	Avg	StdDev	Avg	StdDev	Avg	StdDev	
MoO ₃	BDL	BDL	BDL	BDL	BDL	BDL	BDL	BDL	BDL	BDL	BDL	BDL	0.15
SiO ₂	20.3	0.3	19.8	0.2	19.6	0.3	19.1	0.4	18.6	0.3	27.6	0.4	0.06
ZrO ₂	0.57	0.11	0.54	0.11	0.62	0.12	1.16	0.11	1.53	0.17	7.03	0.44	0.10
B ₂ O ₃	3.18	0.17	2.81	0.17	2.38	0.11	1.87	0.17	4.68	0.33	3.49	0.26	0.10
Al ₂ O ₃	BDL	BDL	BDL	BDL	BDL	BDL	BDL	BDL	0.48	1.38	1.18	0.67	0.06
CaO	10.24	0.39	9.75	0.21	9.38	0.18	9.48	0.20	10.17	0.45	4.75	0.47	0.02
Na ₂ O	BDL	BDL	0.11	0.08	BDL	BDL	BDL	BDL	BDL	BDL	BDL	BDL	0.08
RE ₂ O ₃	66.6	0.9	66.7	0.8	68.8	0.4	67.5	0.5	66.4	5.6	57.0	3.3	0.11
Total	101.0		99.8		100.8		99.2		102.0		101.2		

814

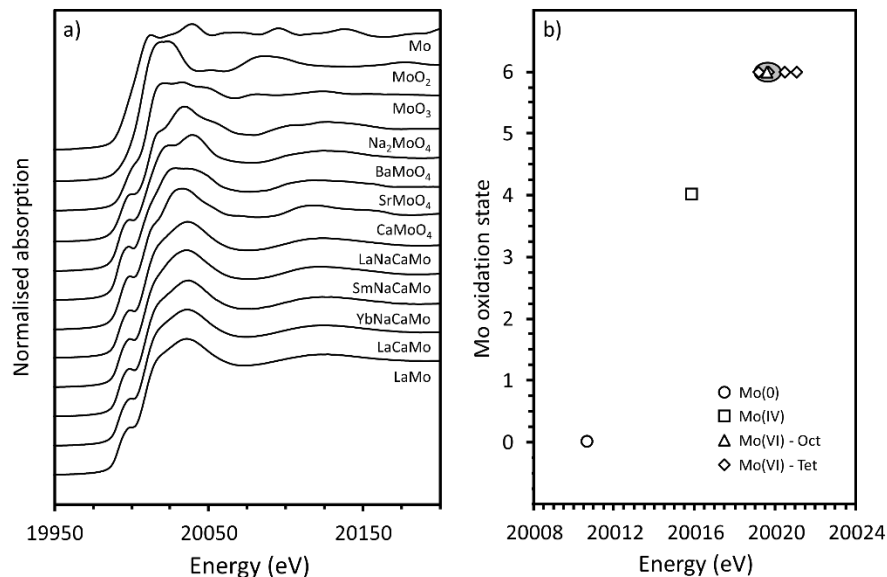
815



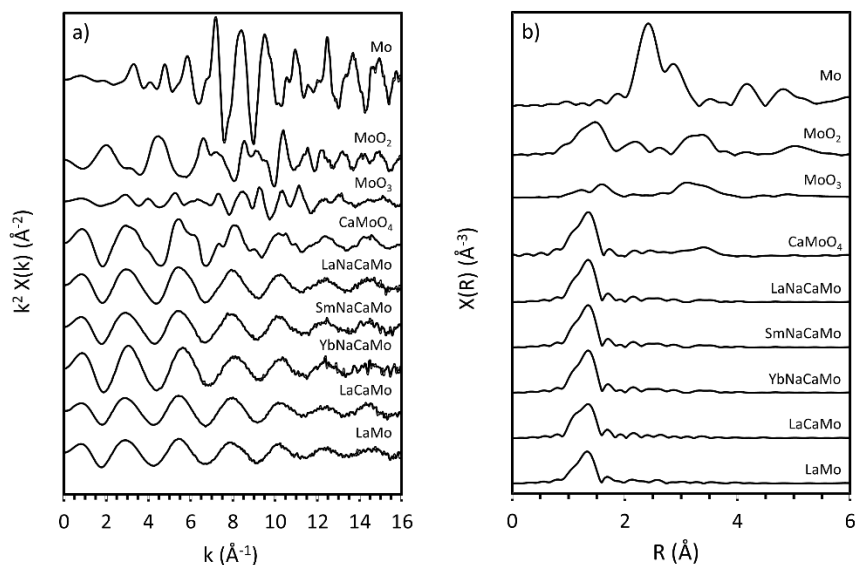
817
818 **Fig. 1.** XRD plot of all quenched samples (after remelt).
819



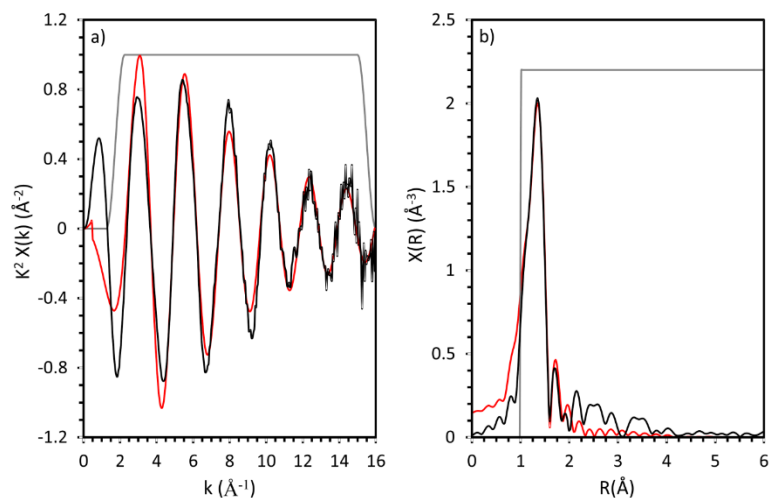
820
821 **Fig. 2.** Normalized Raman spectra of all samples, including a reference spectrum of CaMoO_4
822 (powellite).
823
824



825
 826 **Fig. 3.** Analysis of the Mo K-edge position. a) Normalized Mo K-edge XANES data for glass
 827 samples; spectra for reference standards are included. b) Relationship between the K-edge
 828 position (defined as the energy where the edge jump is equal to 0.8) and the Mo oxidation state;
 829 data points for the glass samples all sit within the grey ellipse.



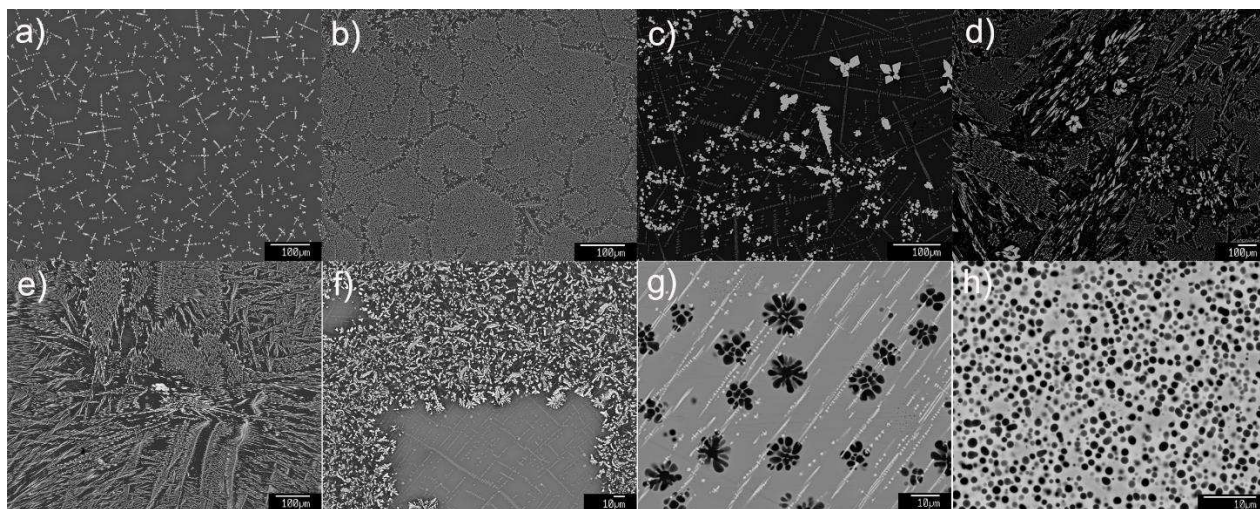
830
 831 **Fig. 4.** EXAFS spectra for the glasses and selected reference standards. a) Normalised k^2 -
 832 weighted spectra and b) Fourier transforms of k^2 -weighted spectra (RDF).



833

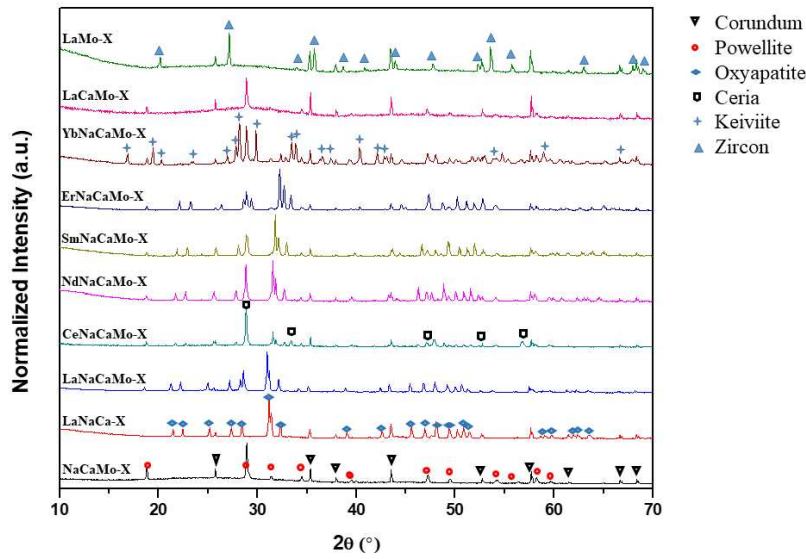
834 **Fig 5.** EXAFS spectra for LaNaCaMo; a) normalised k^2 -weighted spectra and b) Fourier
 835 transforms of k^2 -weighted spectra (RDF). The black line represents the experimental data and
 836 the red line represents the theoretical fit. Fitting window is indicated by solid grey line.

837



838 **Fig. 6.** BSE images of the selected samples; not different scales on some images: a) NaCaMo-X,
 839 b) LaNaCaMo-X, c) CeNaCaMo-X, d) NdNaCaMo-X, e) ErNaCaMo-X, f) YbNaCaMo-X, g)
 841 LaCaMo-X, h) LaMo-X; further images are provided in Supplementary Information.

842

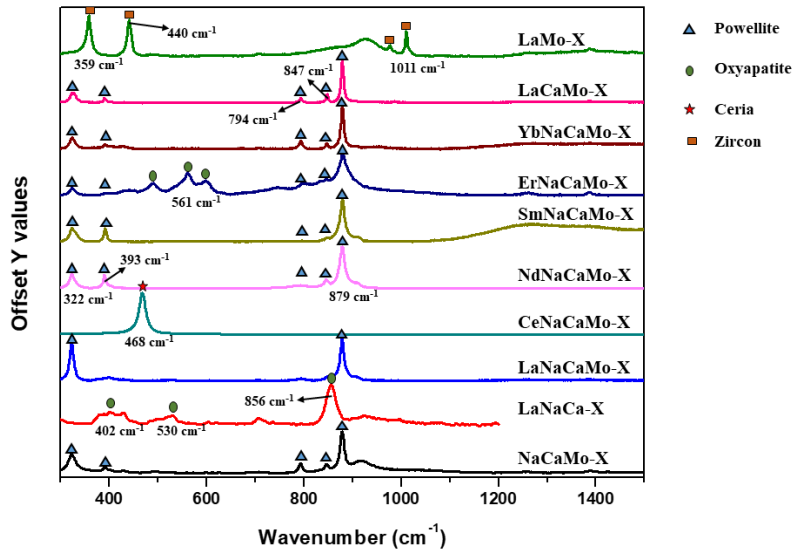


843

844 **Fig. 7.** XRD pattern of all heat - treated samples with corundum added as an internal reference
 845 for quantitative purpose. X-axis shows angle for Cu tube excitation.

846

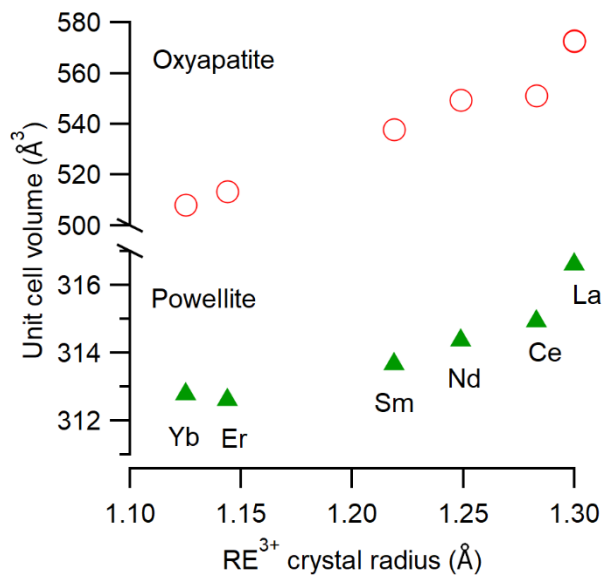
847



848

849 **Fig. 8.** Raman spectra of all heat-treated samples. The each symbol represent the characteristics
 850 peaks for corresponding phase.

851



852

853 **Fig. 9.** Unit cell volumes of oxyapatite and powellite crystals from Rietveld refinement as a
 854 function of RE crystal radii, with coordination number 8 assumed for the RE.

855

856

857

858 **Supplementary Material**

859 Includes photos of selected samples, additional Raman and XAS details and discussion, SEM-BSE of
860 glasses, additional SEM-BSE of glass-ceramics, EPMA analytical conditions, Rietveld refinements, and
861 WDS maps.

862

863